Chemical Science

ROYAL SOCIETY OF CHEMISTRY

EDGE ARTICLE

View Article Online
View Journal | View Issue

Cite this: *Chem. Sci.*, 2022, **13**, 7863

All publication charges for this article have been paid for by the Royal Society of Chemistry

Received 4th March 2022
Accepted 10th June 2022

DOI: 10.1039/d2sc01306a

rsc.li/chemical-science

A machine learning protocol for revealing ion transport mechanisms from dynamic NMR shifts in paramagnetic battery materials†

Min Lin, [a] Jingfang Xiong,[a] Mintao Su,[a] Feng Wang,[a] Xiangsi Liu, [a] Yifan Hou,[a] Riqiang Fu, [d] Yong Yang *[ab] and Jun Cheng *[ac]

Solid-state nuclear magnetic resonance (ssNMR) provides local environments and dynamic fingerprints of alkali ions in paramagnetic battery materials. Linking the local ionic environments and NMR signals requires expensive first-principles computational tools that have been developed for over a decade. Nevertheless, the assignment of the dynamic NMR spectra of high-rate battery materials is still challenging because the local structures and dynamic information of alkali ions are highly correlated and difficult to acquire. Herein, we develop a novel machine learning (ML) protocol that could not only quickly sample atomic configurations but also predict chemical shifts efficiently, which enables us to calculate dynamic NMR shifts with the accuracy of density functional theory (DFT). Using structurally well-defined P2-type $Na_{2/3}(Mg_{1/3}Mn_{2/3})O_2$ as an example, we validate the ML protocol and show the significance of dynamic effects on chemical shifts. Moreover, with the protocol, it is demonstrated that the two experimental ^{23}Na shifts (1406 and 1493 ppm) of P2-type $Na_{2/3}(Ni_{1/3}Mn_{2/3})O_2$ originate from two stacking sequences of transition metal (TM) layers for the first time, which correspond to space groups $P6_3/mcm$ and $P6_322$, respectively. This ML protocol could help to correlate dynamic ssNMR spectra with the local structures and fast transport of alkali ions and is expected to be applicable to a wide range of fast dynamic systems.

Introduction

The wide application of electric vehicles constantly calls for higher power densities of rechargeable batteries, which require faster alkali-ion diffusion in cathode materials with the structural framework of transition-metal oxides (TMOs).[1,2] Hence, understanding the relationship between the atomic structures of cathode materials and alkali-ion diffusions is vitally important.

In contrast to diffraction techniques[3,4] that are sensitive to long-range and ordered structural features, solid-state nuclear magnetic resonance (ssNMR)[5,6] spectroscopy is a unique tool to detect the time-dependent local structures of battery materials. For TMO-based cathode materials, the interpretation of NMR spectra proves very challenging, as the unpaired electrons of TM ions have complicated interactions with the nucleus for which NMR is being observed, resulting in the so-called paramagnetic shifts.[7] To this end, the density functional theory (DFT) methodology for calculating paramagnetic shifts has been continuously developed for over a decade.[8–12] Nevertheless, the applications of such state-of-the-art computational methods are restricted to slow alkali-ion dynamic systems, *e.g.*, polyanion-type materials[8–17] or fully lithiated layered materials,[9,18] in which the measured shift corresponds to the local minimum of the potential energy surface (PES) and is characterized by DFT optimized structures (*i.e.*, 0 K). However, for high-rate cathode materials, the fast alkali-ion hopping between distinct chemical sites typically results in fast chemically exchanged NMR spectra at room temperature (RT), named dynamic NMR spectra,[19] which represent the weighted average of the chemical shifts of all of the alkali-ion environments involved in chemical exchange.[20] Since the dynamic NMR spectra result from the correlated effect between the local environments of the alkali ion and its dynamics, it is extremely difficult to accurately extract the structural information from the dynamic NMR spectra directly through DFT calculations. To the best of our knowledge, there is not yet a rigorous and applicable first-principles methodology for calculating the dynamic NMR shifts of paramagnetic battery materials.

Dynamic NMR spectra have been extensively observed in cathode materials of sodium-ion batteries (SIBs). The ^{23}Na

[a]*Collaborative Innovation Center of Chemistry for Energy Materials, State Key Laboratory for Physical Chemistry of Solid Surface, College of Chemistry and Chemical Engineering, Xiamen University, Xiamen 361005, China. E-mail: yyang@xmu.edu.cn*

[b]*College of Energy, Xiamen University, Xiamen 361005, China*

[c]*Innovation Laboratory for Sciences and Technologies of Energy Materials of Fujian Province (IKKEM), Xiamen 361005, China. E-mail: chengjun@xmu.edu.cn*

[d]*National High Magnetic Field Laboratory, 1800 E. Paul Dirac Drive, Tallahassee, FL 32310, USA*

† Electronic supplementary information (ESI) available. See https://doi.org/10.1039/d2sc01306a.

spectra of P-type (Delmas *et al.*'s notation[21]) SIB cathode materials are usually dynamic NMR spectra at RT,[22–30] due to the large layer spacing that enables fast Na^+ diffusion. Even though P2-type $Na_{2/3}(Ni_{1/3}Mn_{2/3})O_2$ has been intensively studied,[31] controversy still exists regarding the ^{23}Na NMR spectra of the as-synthesized materials. Wu *et al.*[24] observed two ^{23}Na shifts in the paramagnetic region, with the dominating one assigned to the P2 phase and the weaker signal with a lower shift to the sodium-poor phase. In contrast, Clément *et al.*[22] assigned the lower shift (1422 ppm) to stacking faults of the O2 phase (Delmas *et al.*'s notation[21]). In principle, lowering the temperature could be an option to slow down the exchange dynamics in order to resolve the local environments of the Na^+ and its dynamic behind the NMR spectra. For instance, Mukhamedshin *et al.*[29] observed the ^{23}Na shifts of distinct sites of P2-type $Na_{0.67}CoO_2$ in a static NMR experiment below 150 K, which required significant effort in material synthesis to provide aligned single-phase powder samples. However, such a low temperature is not typically available in high-resolution magic-angle-spinning (MAS) ssNMR measurements, where a fast spinning is acquired to obtain high-resolution NMR spectra of powdered paramagnetic battery samples.

Very recently, utilizing highly efficient machine learning potential molecular dynamic (MLPMD)[32] simulations that enable sufficient sampling of alkali-ion hopping events, we tentatively calculated the dynamic ^{23}Na NMR shift of P2-type $Na_{2/3}(Mg_{1/3}Mn_{2/3})O_2$ for the first time.[20] Nevertheless, the DFT calculation of the ^{23}Na shift is still based on certain optimized (*i.e.*, 0 K) Na^+ patterns due to the high computational cost of chemical shifts. This infantile method neglects the thermal fluctuation effect on the chemical shifts, which limits its wide application. Therefore, developing a solid and widely applicable computational method for dynamic NMR spectra is urgent and important.

In this work, we developed a novel machine learning (ML) protocol for calculating dynamic NMR shifts. Fig. 1 shows a schematic illustration of the protocol that involves two ML models, an MLP model for accelerating configuration sampling, and a Neural Network (NN) model for fast chemical shift prediction, named the NN-NMR model. Specifically, we adopted the well-developed Deep Potential Generator (DP-GEN) scheme[33,34] for generating the MLP, which explores new configurations with a concurrent learning approach, and the so-called deep potential (DP)[32,35] model is trained iteratively until it reaches the DFT level accuracy. After sufficient sampling of the alkali-ion hopping related to dynamic NMR spectra with long-time DPMD simulations, the chemical shift datasets are generated with sparse configurations of DPMD simulation trajectories and the DFT method. Then, using the smooth overlap of atomic positions (SOAP)[36,37] descriptors of local structures and chemical shifts as the input layer and output layer of the NN, respectively (Fig. 2a), the NN-NMR model is trained and tested with the DFT dataset of chemical shifts. Finally, the chemical shifts of dense configurations in DPMD simulation trajectories are predicted using the NN-NMR model.

We calculated the dynamic ^{23}Na NMR shift of P2-type $Na_{2/3}(Mg_{1/3}Mn_{2/3})O_2$ (hereafter denoted as P2-NMMO),[38–41] and compared the results with previous computational and experimental results[20] for validating the ML protocol. The well-trained NN-NMR model shows highly computational efficiency and accuracy for predicting chemical shifts. Besides, combining with experiments and the dynamic ^{23}Na shifts of P2-type $Na_{2/3}(Ni_{1/3}Mn_{2/3})O_2$ (hereafter denoted as P2-NNMO) calculated with the protocol, we demonstrated that the lower ^{23}Na shift being debated can be attributed to the averaged ^{23}Na shift of $P6_3/mcm$ NNMO (Fig. S1a and b†),[42] thus clarifying its structural assignment.

Methods

The computational formalism of chemical shifts

The isotropic ^{23}Na shift of a paramagnetic system is composed of four parts, Fermi-contact shift (δ_{FC}), pseudo-contact shift

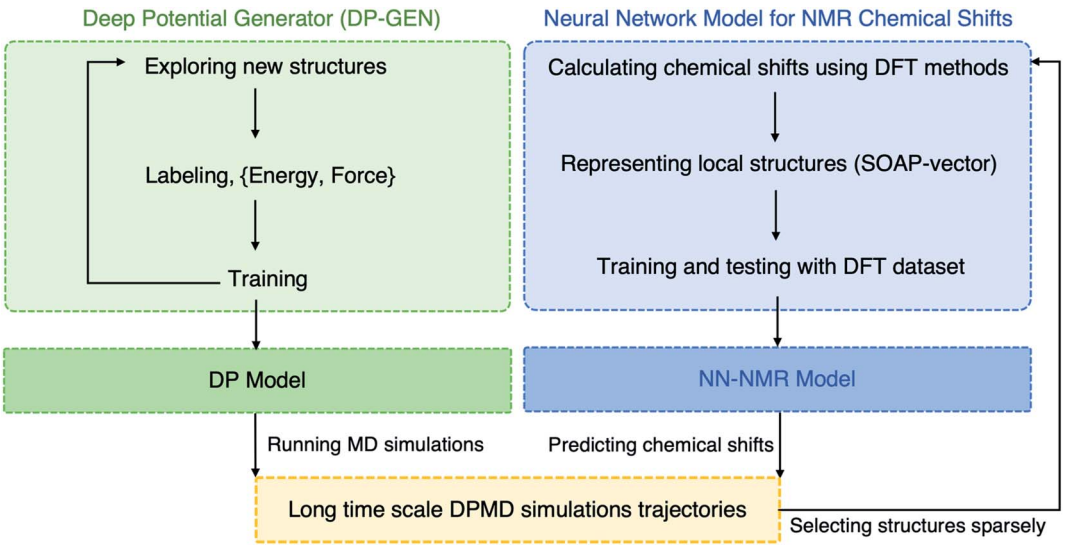

Fig. 1 Schematic illustration of the machine learning (ML) protocol for calculating the dynamic NMR chemical shifts.

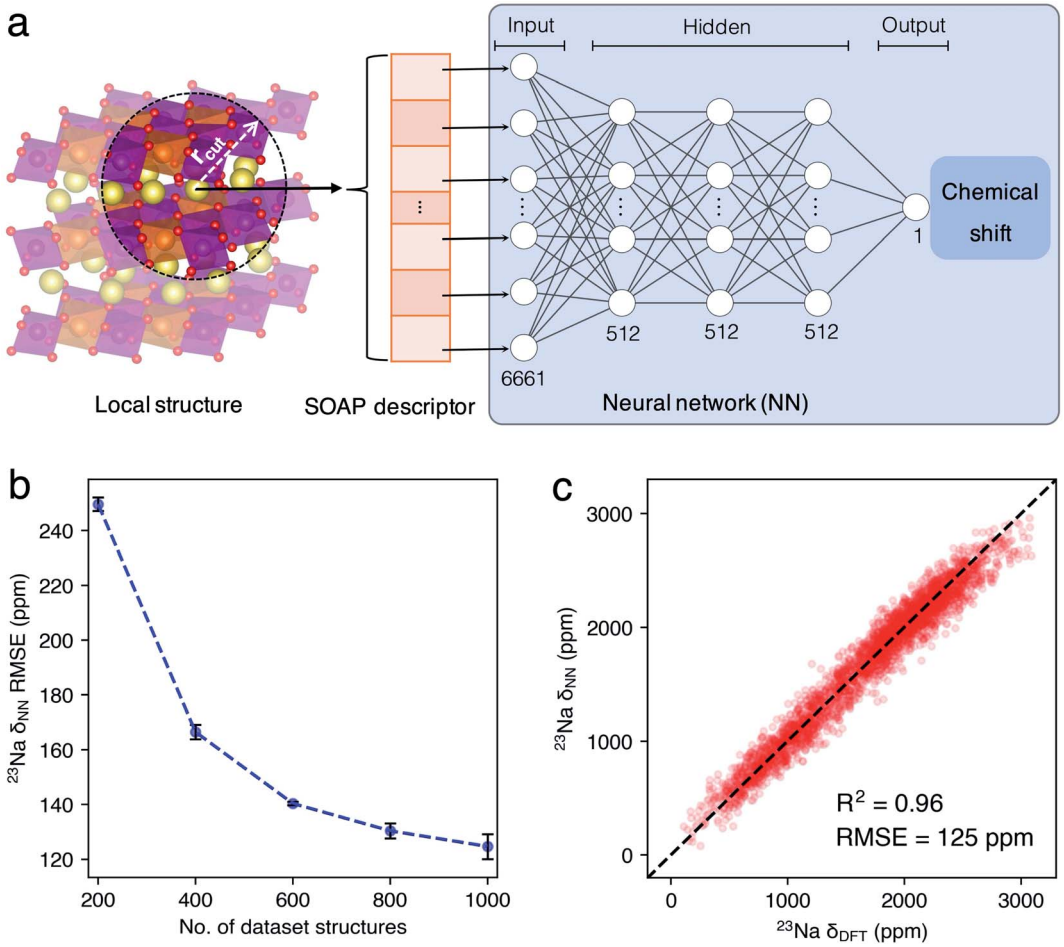

Fig. 2 (a) Illustration of the NN-NMR model for predicting chemical shifts. A Na^+ local environment in the supercell model of $P6_3/mcm$ $Na_{2/3}(Mg_{1/3}Mn_{2/3})O_2$ is shown as an example, and the No. of nodes in each layer of the NN-NMR model was labeled. (b) The testing set RMSEs between ^{23}Na δ_{DFT} and δ_{NN} of P2-$Na_{2/3}(Mg_{1/3}Mn_{2/3})O_2$ evolute with the No. of dataset structures. The black error bars indicate the standard deviations (STDs) of the RMSEs. (c) The correlation of ^{23}Na δ_{DFT} and δ_{NN}. The dashed black line indicates a perfect correlation.

(δ_{PC}), orbital shift (δ_{orb}) and second-order quadrupole shift (δ_{QIS}).[7,43] Meanwhile, previous studies of the ^{23}Na shift of P2-NMMO and P2-NNMO showed that δ_{FC} dominates the total shift.[20,22] It is worth noting that δ_{QIS} is inversely proportional to the square of the magnetic field strength, and herein 9.4 T suppresses the δ_{QIS} of P2-NMMO and P2-NNMO on the order of tens of ppm.[20] Therefore, we only calculated δ_{FC} with DFT methods (*i.e.*, $\delta_{DFT} = \delta_{FC}$), given by:[8,16]

$$\delta_{FC} = \frac{A}{\hbar\gamma_I} \frac{{\mu_{eff}}^2}{g_e\mu_B 3k(T-\Theta)} \quad (1)$$

where A, $\hbar$, γ, g_e, μ_B, k, and T are the hyperfine coupling constant, Planck's constant, nuclear gyromagnetic ratio, free-electron g-factor and Bohr magneton, Boltzmann constant, and Kelvin temperature, respectively. Besides, the effective magnetic moment of the paramagnetic center (μ_{eff}) and Curie–Weiss constant (Θ) were extracted from magnetic susceptibility measurements (Fig. S6†), to incorporate spin–orbital coupling (SOC) and residual exchange coupling effects,[7,8] respectively. A reduced hyperfine coupling constant (A^I_{iso}) outputted in the Vienna *Ab initio* Simulation Package (VASP)[44,45] is described by ref. 46 and 47:

$$A^I_{iso} = \frac{2}{3}\frac{\mu_0\gamma_e\gamma_I}{\langle S_z\rangle}\delta\int\delta_T(\mathbf{r})\rho_s(\mathbf{r}+\mathbf{R}_I)d\mathbf{r} \quad (2)$$

where ρ_s, μ_0, γ_e, and $\delta_T(\mathbf{r})\rho_s$ are the spin density, the magnetic susceptibility of free space, the electron gyromagnetic ratio, and a smeared out δ function,[46] respectively. A^I_{iso} is the reduced form of A by the expectation value of the z-component of the total electronic spin, $\langle S_z\rangle$, *i.e.*, $A = A^I_{iso}\langle S_z\rangle$.

Density functional theory calculations

All DFT calculations were performed by using VASP[44,45] version 5.4.4. with the Projector Augmented Wave (PAW) method.[48] For generating the datasets of DP and NN-NMR models, the convergence criterion of self-consistent field (SCF) iterations, *K*-point, Na pseudopotential, and cut-off energy of the plane-wave basis set is 10^{-5} eV, 2 × 2 × 2, *Na_pv*, and 400 eV, respectively (Fig. S3†). The

total energies and atomic forces were calculated with the Perdew–Burke–Ernzerhof (PBE)[49] functional. To better describe the electronic structures of TM ions that have significant effects on δ_{FC}, the hyperfine coupling constant was calculated with the Strongly Constrained and Appropriately Normed[50] (SCAN) functional. $2 \times 2 \times 1$ supercell models with 88 atoms were utilized for both NMMO and NNMO, and the cell parameters were fixed as experimental results.[20]

To reasonably compare the total energies of all types of NMMO supercell models (Fig. 4c), the cell parameters and atomic positions were fully relaxed with a higher cut-off energy of 520 eV that provides more accurate stress tensors. The P2 phase supercell adopted the well-known large-zigzag (LZZ, Fig. S1d†)[51,52] Na^+ pattern. The O2 supercell adopted a honeycomb (Fig. S1e†) Na^+ pattern that has the lowest coulomb energy among enumerated structures implemented in the *Supercell*[53] program.

Deep potential training and deep potential molecular dynamics simulations

Since the 200 nanoseconds (ns) DPMD simulation trajectories of P2-NMMO with DFT level accuracy were accomplished in our previous study,[20] we directly utilized these trajectories to generate their ^{23}Na δ_{DFT} dataset. The DP model of P2-NNMO was also trained in DP-GEN software[33] with the same protocol as that of P2-NMMO described in detail in ref. 20 and 33. After six iterations of training, exploration and labeling, 1386 configurations were included in the dataset. The DPMD simulations of supercell models of $P6_3/mcm$ and $P6_322$ NNMO were carried out by using the LAMMPS[54] package with an NVT ensemble at 300 K for 200 ns. All DPMD simulations started with the LZZ Na^+ patterns and the time step was 1 femtosecond (fs).

The NN-NMR model for predicting chemical shifts

For each trajectory, 500 configurations with a time interval of 400 picoseconds (ps) were extracted and labeled, and thus the DFT datasets of P2-NMMO or P2-NNMO contain 1000 configurations and 16 000 ^{23}Na shifts. The SOAP[36] vectors of Na^+ local environments were generated with the QUIP package and *quippy*[55] interface. The cutoff of the Na^+ local region (r_{cut}), the standard deviation of the Gaussian (σ), the number of radial basis functions (n_{max}), and the maximum degree of spherical harmonics (l_{max}) are 5.5 Å, 0.5 Å, 9, and 9, respectively. The initialization and training of the NN-NMR model were implemented in Tensorflow[56] with the Keras[57] Application Program Interface (API). The hidden layer of the NN-NMR model has three sequential layers with 512 nodes per layer (Fig. 2a). Dropouts with a rate of 0.1 and an L2 regularization with $\lambda = 1 \times 10^{-2}$ were applied to every layer of the NN-NMR model. The learning rate starts with 10^{-3} and decays inversely during every echo with a decay rate of 5. The total no. of echo is 2000. We performed a 5-fold cross-validation with a training/testing set fraction of 0.8 : 0.2 for all NN-NMR models. An early stop scheme was applied for preventing overfitting. Our encoded training and testing processes of the NN-NMR model are also available at **https://github.com/chenggroup/nmr**.

Results and discussion

Validation of the ML protocol with P2-type $Na_{2/3}(Mg_{1/3}Mn_{2/3})O_2$

Given that our previous work[20] demonstrated that the two ^{23}Na peaks of P2-NMMO, located at 1522 and 1665 ppm, are in-layer dynamic averaged ^{23}Na shifts in space groups $P6_3/mcm$ and $P6_322$, which correspond to two stacking sequences of transition metal layers, Mg^{2+} ions stack linearly (Fig. S1b†) and staggered (Fig. S1c†) along the *z*-axis with a Mg^{2+}/Mn^{4+} honeycomb superstructure (Fig. S1a†), respectively. In this section, we take P2-NMMO as an example for validating our ML protocol and the NN-NMR model, computational procedures and parameters were presented in the Introduction and Methods sections. Fig. 2b shows that the root-mean-square errors (RMSEs) between the ^{23}Na shift of the testing set calculated with the DFT method (δ_{DFT}) and with the NN-NMR model (δ_{NN}) decrease with the number (No.) of dataset structures. When No. is 1000, the mean value of 5-fold cross-validation RMSEs is 125 ppm with an *R* square factor (R^2) of 0.96. Given that the ^{23}Na shift of P2-NMMO approximately ranges from 0 to 3000 ppm, an RMSE of 125 ppm indicates that the NN-NMR model of P2-NMMO is highly accurate (Fig. 2c). Besides, the NN-NMR model is also highly efficient; the ^{23}Na δ_{NN} of 50 000 configurations taken from 200 ns DPMD trajectories was predicted on an NVIDIA GeForce RTX2080 Ti GPU within 40 minutes, which would take around one year using the DFT method on a single node composed of 28 parallel Intel Xeon E5-2680 v4 CPU cores. The prediction speed of the NN-NMR model is limited by a constant I/O overhead, and the prediction time of a configuration linearly scales with the No. of atoms.

For 50 000 configurations in each DPMD trajectory of $P6_3/mcm$ and $P6_322$ NMMO, Fig. 3a shows the histograms of ^{23}Na δ_{NN} separately. δ_{NN} is mainly distributed between 0 and 3000 ppm, and the histograms are composed of several broad Gaussian peaks, suggesting that the dynamic effect on the ^{23}Na shift is significant. Benefiting from the sufficient configurations of the DP model and ^{23}Na shift sampling of the NN-NMR model, the statistic errors of *xy*-plane averaged ^{23}Na δ_{NN} decrease to sub-ppm (Fig. S10a†). The averaged ^{23}Na δ_{NN} of $P6_3/mcm$ and $P6_322$ is 1638 and 1763 ppm, respectively, which could conclude the same assignment as our previous work.[20]

To assign the Gaussian peaks of ^{23}Na δ_{NN} histograms and understand the difference between the averaged ^{23}Na shift of $P6_3/mcm$ and $P6_322$, we further analyzed the spatial distributions of the ^{23}Na shift. Given that the Na^+ diffusion paths of P2-NMMO are two-dimensional (2D, *xy*-plane) channels, the grid averaged ^{23}Na δ_{NN} on the *xy*-plane could represent the spatial distributions of the ^{23}Na shift (Fig. 3b and c), and the standard deviations (STDs) of ^{23}Na δ_{NN} within the grids are also shown in Fig. S8a and b.† Then, the site-centered circles with a radius of 0.8 Å were utilized for defining the boundaries for all Na sites, and they include most Na^+ without double counting, as verified by the finding that the sum of δ_{NN} histograms of Na sites approximates to the δ_{NN} histogram of the space group (Fig. 3a). By this means, the Na^+ occupation fractions and the centered

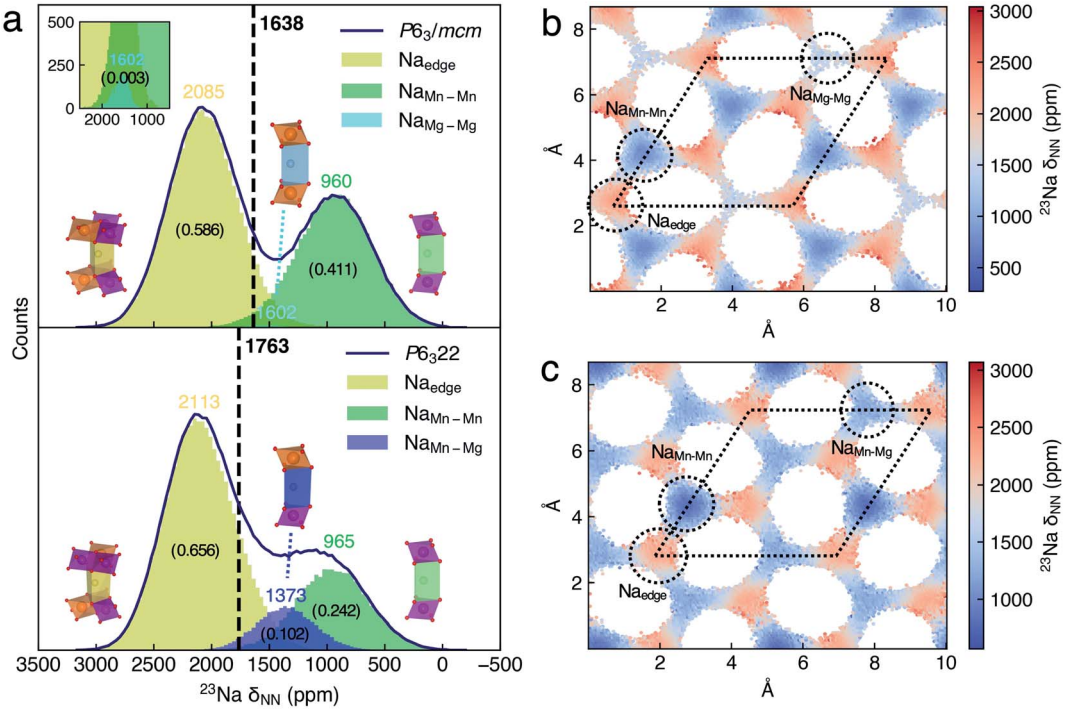

Fig. 3 (a) Histograms of the ^{23}Na δ_{NN} distribution of Na sites in P2-$Na_{2/3}(Mg_{1/3}Mn_{2/3})O_2$. The black curves indicate the histogram outlines of the ^{23}Na δ_{NN} of $P6_3/mcm$ and $P6_322$ $Na_{2/3}(Mg_{1/3}Mn_{2/3})O_2$. The local structures of Na sites are inseted along with their shift histogram, and a scaled histogram for highlighting Na_{Mg-Mg} sites is also inseted. The averaged ^{23}Na δ_{NN} of space groups is indicated by the black vertical lines. The averaged δ_{NN} of the Na site and space group is labeled, and the occupation fractions of Na sites were labeled with numbers in brackets. The *xy*-plane ^{23}Na δ_{NN} distribution maps of (b) $P6_3/mcm$ and (c) $P6_322$ $Na_{2/3}(Mg_{1/3}Mn_{2/3})O_2$. The dotted circles and rhombi indicate Na sites and unit cells, respectively.

δ_{NN} of distinct Na sites can be quantified. In $P6_3/mcm$, the centered ^{23}Na δ_{NN} of Na_{edge}, Na_{Mn-Mn}, and Na_{Mg-Mg} sites is 2085, 960, and 1602 ppm with the occupation fractions of 0.586, 0.411, and 0.003, respectively. In $P6_322$, the Na_{edge} (2113 ppm) and Na_{Mn-Mn} (965 ppm) shifts, and their Gaussian distributions well agree with those of $P6_3/mcm$. Moreover, the Na_{Mn-Mg} site shifts (1373 ppm) approximate to the middle point (1284 ppm) of Na_{Mn-Mn} and Na_{Mg-Mg} site shifts in $P6_3/mcm$, which is consistent with the additive character of δ_{FC}.[9] Therefore, the lower occupation fraction of the lowest shift site (Na_{Mn-Mn}) and the higher occupation fraction of the highest shift site (Na_{Mn-Mn}) mainly contribute to the higher averaged ^{23}Na shift of $P6_322$.

In our previous method,[20] the ^{23}Na shifts of Na sites were calculated with the DFT optimized (*i.e.*, 0 K) LLZ Na^+ pattern (Table 1, δ_{LZZ}), and the averaged shift of the space group is the occupation weighted shift of distinct Na sites, which neglected the dynamic effect on the ^{23}Na shifts. To clarify the significance of the dynamic effect, we calculated the δ_{LZZ} with the DFT method and compared it to the centered ^{23}Na δ_{NN} of Na sites. Except for the δ_{LZZ} of the Na_{edge} site (2102–2160 ppm) that approximates to its centered ^{23}Na δ_{NN}, the δ_{LZZ} of Na_{Mn-Mn}, Na_{Mg-Mg}, and Na_{Mn-Mg} sites is 503, 1494, and 1052 ppm, which are considerably lower than their centered ^{23}Na δ_{NN}, 960, 1602, and 1373 ppm, respectively. As a result, the averaged shifts of $P6_3/mcm$ and $P6_322$ calculated with the LZZ pattern are 1452 and 1640 ppm, which are lower than those (1638 and 1763 ppm) calculated with the ML protocol, respectively. Given that experimental shifts[20] are 1552 ppm ($P6_3/mcm$) and 1665 ppm ($P6_322$), the overestimated shifts of the ML protocol probably are attributed to the errors of the SCAN functional. Comparing with the experimental shift difference (143 ppm) of the two space groups, the ML protocol (125 ppm) gives a better agreement than that calculated with the LZZ pattern (188 ppm). Besides, the ML protocol could calculate the dynamically averaged NMR shift without defining alkali-ion sites, which enables its wide application. For instance, the super-ionic conductors (SICs) that typically have three-dimensional (3D) alkali-ion transport channels and flexible structural frameworks,[58] or even electrolytes, in which the alkali-ion sites are not always well defined. It should be noted that most SICs and electrolytes are diamagnetic, and the computational method of their chemical shifts is different from that of paramagnetic electrodes.[59] Moreover, the time-averaged ^{23}Na δ_{NN} simulated with different periods of time indicates how the shifts of distinct sites merge into the dynamic NMR shift (Fig. S11†).

Revealing the fine structures of P2-type $Na_{2/3}(Ni_{1/3}Mn_{2/3})O_2$

Since our ML protocol was successfully validated in P2-NMMO, herein, we extended its application to rationally assign the debated dynamic ^{23}Na NMR shift of as-synthesized P2-NNMO.[22,24] Firstly, we synthesized P2-type NNMO with the

Table 1 Computational and experimental ^{23}Na NMR shift of P2-type $Na_{2/3}(Mg_{1/3}Mn_{2/3})O_2$. δ_{LZZ} is a ^{23}Na shift calculated with the LZZ Na^+ pattern, δ_{NN} is the centered ^{23}Na shift predicted with the NN-NMR model and 50 000 configurations, and δ_{exp} is the experimental ^{23}Na shift reported in ref. 20

Space group	Sites	Occupation fractions	δ_{LZZ}/ppm		δ_{NN}/ppm		δ_{exp} (ref. 20)/ppm
$P6_3/mcm$	Na_{Mn-Mn}	0.411	503	1452	960	1638	1522
	Na_{Mg-Mg}	0.003	1494		1602		
	Na_{edge}	0.586	2102–2133		2085		
$P6_322$	Na_{Mn-Mn}	0.242		1640	965	1763	1665
	Na_{Mn-Mg}	0.102	1052		1373		
	Na_{edge}	0.656	2139–2160		2113		

procedure described in ref. 60. As shown in Fig. 4a, the PXRD diffraction signal can be indexed to the space group $P6_3/mmc$, a hexagonal phase with cell parameters $a = b = 2.88915$ Å and $c = 11.14482$ Å, which is consistent with ref. 24, 28, 31, 61 and 62. Fig. 4b shows the MAS NMR ^{23}Na spectra at RT, two isotropic shifts located at 1493 (peak 1) and 1406 (peak 2) ppm that well agree with Clément *et al.*'s[22] results (1510 and 1422 ppm).

To evaluate the thermodynamic stabilities of debated structures[22,24] and other possible structures, we performed DFT calculations of the total energy of related supercell models (see the Methods section). Fig. 4c shows the relative total energies (RTEs) of supercell models by taking the total energy of the $P6_322$ NNMO supercell as a reference. First of all, one Ni^{2+}/Mn^{4+} disordering results in a RTE of 0.40 eV per supercell, agreeing with the Ni^{2+}/Mn^{4+} honeycomb superstructure that was evidenced by neutron diffraction (ND).[63] Second, the O2 phase is thermodynamically very unstable with a RTE of 2.74 eV per supercell. Besides, the simulated PXRD patterns of a randomly mixed $P6_322$–$P6_3/mc$ (P2–O2) structure show that a 10–20% mixing O2 phase could lead to remarkable broadening of (004), (104), and (106) peaks (Fig. S12†), which was not observed in the recorded PXRD pattern (Fig. 4a). Therefore, the O2 phase is unlikely to exist in as-synthesized P2-NNMO and was excluded from further investigations. Finally, $P6_3/mcm$ has a very close RTE (0.04 eV per supercell) with $P6_322$, indicating the possibility of a mixture of $P6_3/mcm$ and $P6_322$. Note that both $P6_3/mcm$ and

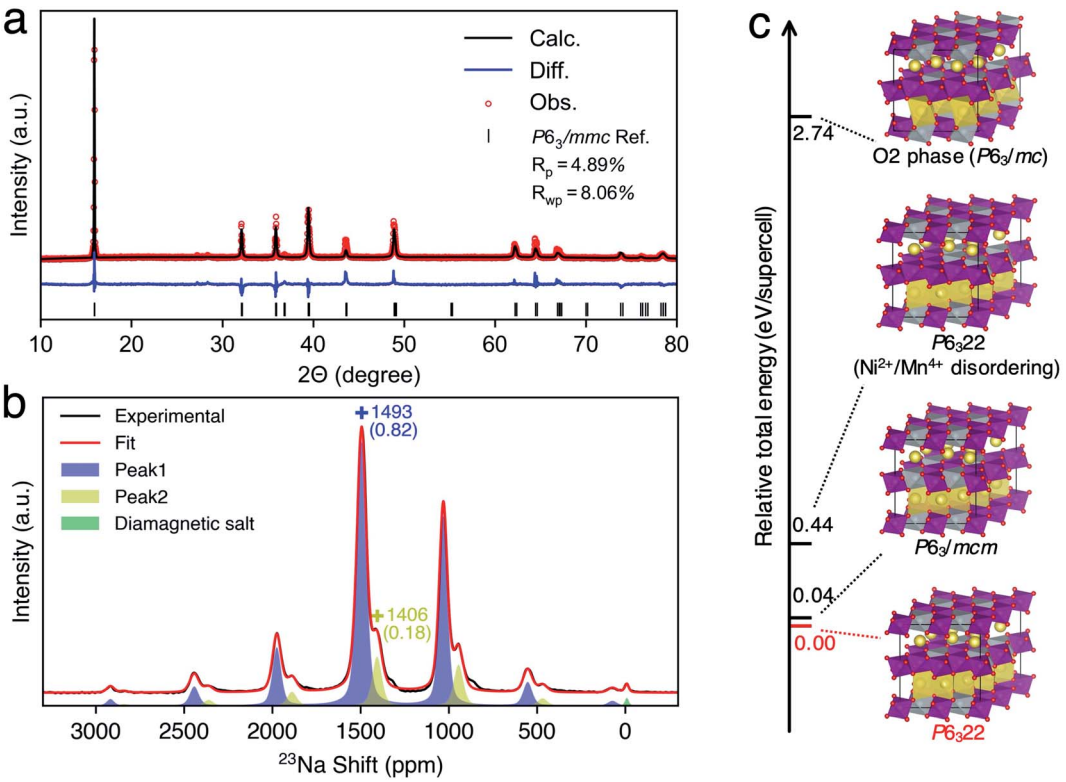

Fig. 4 (a) PXRD of P2-type $Na_{2/3}(Ni_{1/3}Mn_{2/3})O_2$ and its refinement. The fitting good parameters R_p and R_{wp} are labeled. (b) The ^{23}Na MAS ssNMR spectra of P2-type $Na_{2/3}(Ni_{1/3}Mn_{2/3})O_2$ and fitting curves, in which the peaks of isotropic shifts are labeled with "+", and the shift and its fractions are labeled with colored numbers without and with brackets, respectively. (c) Supercell structures of $Na_{2/3}(Ni_{1/3}Mn_{2/3})O_2$ and their relative total energies (RTEs). For clarification, only underlayer Na prisms were shown in all structures.

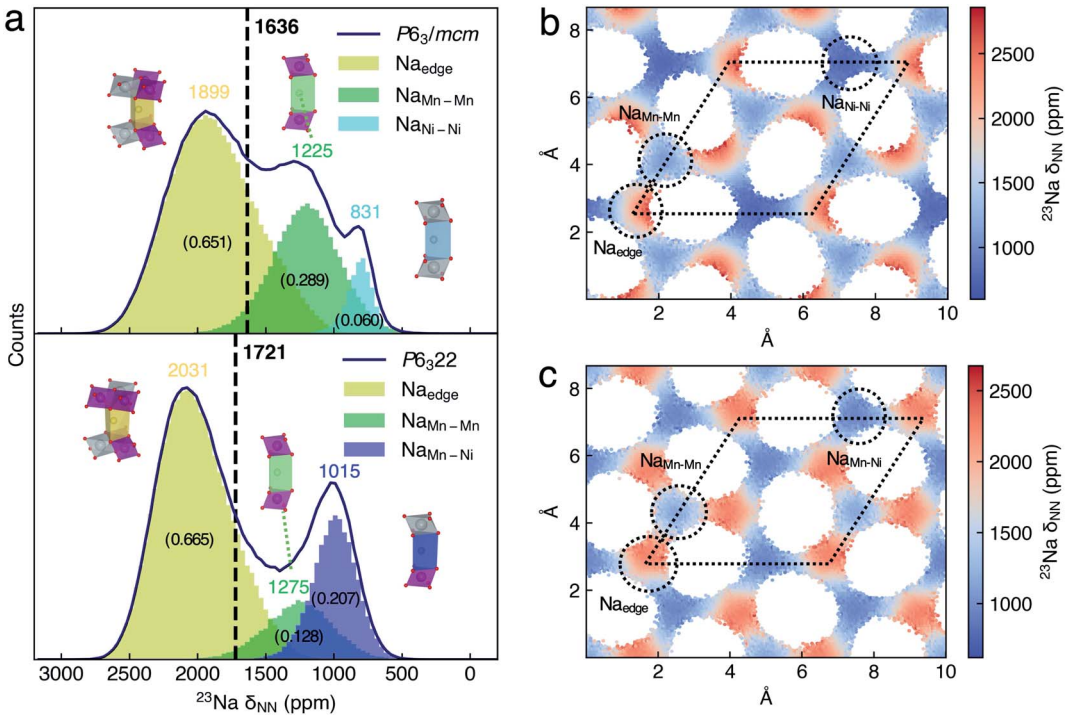

Fig. 5 (a) Histograms of the ^{23}Na δ_{NN} distribution of Na sites in P2-$Na_{2/3}(Ni_{1/3}Mn_{2/3})O_2$. The black curves indicate the histogram outlines of the ^{23}Na δ_{NN} of $P6_3/mcm$ and $P6_322$ $Na_{2/3}(Ni_{1/3}Mn_{2/3})O_2$. The local structures of Na sites are inseted along with its shift histogram. The averaged ^{23}Na δ_{NN} of space group is indicated by black vertical lines. The number of averaged δ_{NN} for the Na site and space group is labeled, and the occupation fractions of Na sites are labeled with the numbers in brackets. The *xy*-plane ^{23}Na shift distribution maps of (b) $P6_3/mcm$ and (c) $P6_322$ of P2-$Na_{2/3}(Ni_{1/3}Mn_{2/3})O_2$. The dotted circles and rhombi indicate Na sites and unit cells, respectively.

$P6_322$ are secondary phases of $P6_3/mmc$ with a prerequisite of a Ni^{2+}/Mn^{4+} honeycomb superstructure, and the superstructure-related XRD peaks should reflect the stacking sequences of TM layers.[20] However, the Ni^{2+}/Mn^{4+} superstructure is invisible for X-rays because Ni^{2+} and Mn^{4+} have similar atomic numbers, and the PXRD patterns of mixed $P6_3/mcm$–$P6_322$ keep constant among all ranges of fraction ratios (Fig. S12†). Therefore, extending the NMR methodology to identify these indistinguishable structures is very useful as an example of a good compensation for PXRD.

To provide the NMR evidence of $P6_3/mcm$–$P6_322$ mixed stacking in P2-NNMO, we applied our novel ML protocol for calculating the dynamic ^{23}Na NMR shift of $P6_3/mcm$ and $P6_322$. Fig. S2† shows that the RMSE of energies and forces between the well-trained DP model and DFT method is $2.80 \times 10^{-4} \pm 6.24 \times 10^{-8}$ eV per atom and $1.24 \times 10^{-2} \pm 2.87 \times 10^{-4}$ eV Å^{-1}, respectively, suggesting that the DP model reaches the DFT level accuracy. For the accuracy of the NN-NMR model, the RMSE and R^2 coefficient of the ^{23}Na shift calculated between with the NN-NMR model and with the DFT method are 83 ppm and 0.97, respectively (Fig. S5†). With the help of the highly accurate and efficient DP and NN-NMR model, the ^{23}Na shifts of 50 000 configurations in 200 ns DPMD simulations were predicted for each space group, and the averaged shift of $P6_322$ and $P6_3/mcm$ is 1721 and 1636 ppm with negligible statistical errors, respectively (Fig. S10b†). Consequently, peak 1 (1493 ppm) and peak 2 (1406 ppm) in Fig. 4b were assigned to the averaged ^{23}Na shift of $P6_322$ and $P6_3/mcm$, respectively. Thus, we concluded that P2-NMMO is composed of a mixed stacking of $P6_322$ and $P6_3/mcm$ with a fraction of 0.82 and 0.18, respectively.

To understand the averaged shift differences of $P6_322$ and $P6_3/mcm$ NNMO, we adopted the same analysis approach as that of P2-NMMO. The Gaussian peaks in ^{23}Na δ_{NN} histograms (Fig. 5a) were assigned according to the *xy*-plane ^{23}Na δ_{NN} maps (Fig. 5b and c). The averaged ^{23}Na δ_{NN} of Na_{edge}, Na_{Mn-Mn}, and Na_{Ni-Ni} sites is 1899, 1225, and 831 ppm with an occupation fraction of 0.651, 0.289 and 0.060 in $P6_3/mcm$, respectively. The averaged ^{23}Na δ_{NN} of Na_{edge}, Na_{Mn-Mn}, and Na_{Mn-Ni} sites is 2031, 1275, and 1015 ppm with an occupation fraction of 0.665, 0.128, and 0.207 in $P6_322$, respectively. It is apparent that the higher Na_{edge} shift of $P6_322$ (2031 ppm) than that of $P6_3/mcm$ (1899 ppm) is the main reason for the higher averaged shift of $P6_322$ P2-NNMO.

The effect of different P2-type stacking sequences ($P6_3/mcm$ and $P6_322$) on Na^+ mobilities

After the stacking sequences of TM layers in P2-type NMMO and NNMO were clearly revealed by combining the NMR experiment and our ML protocol, a remaining question is how these stacking sequences affect Na^+ mobilities. Thanks to sufficient sampling of Na^+ hopping during 200 ns DPMD simulations, the diffusion coefficients of Na^+ (D_{Na}) could be estimated from the root-mean-square-displacement (RMSD) of Na^+ with a minor STD[64] (Fig. S9a and b†). Interestingly, the D_{Na} of $P6_3/mcm$

NMMO (1.0×10^{-7} cm^2 s^{-1}) is lower than that of $P6_322$ NMMO (4.4×10^{-7} cm^2 s^{-1}) by over four times,[20] while the D_{Na} of $P6_322$ NNMO (1.0×10^{-6} cm^2 s^{-1}) is similar to that of $P6_3/mcm$ NNMO (9.6×10^{-7} cm^2 s^{-1}). To understand the difference between NMMO and NNMO, we proposed a significant blockage effect of Mg^{2+} on Na^+ diffusion. Fig. S7† shows the *xy*-plane Na^+ distribution maps of P2-type NMMO and NNMO obtained from DPMD trajectories, showing honeycomb Na^+ diffusion channels. In $P6_3/mcm$ NMMO, low Na^+ occupation of Na_{Mg-Mg} sites indicates a blockage effect of Mg^{2+} on Na^+ diffusion, and the blockage effect is mitigated in $P6_322$ NMMO since Mg^{2+} is staggered along the *z*-axis (Fig. S1c†), resulting in a higher D_{Na}. In contrast, Ni^{2+} has no such blockage effect on the Na^+ diffusion of P2-NNMO as the occupations of Na_{Ni-Ni} and Na_{Mn-Mn} sites are similar in $P6_3/mcm$ NNMO. Therefore, the staggered arrangement of Ni^{2+} in $P6_322$ NNMO cannot significantly improve the D_{Na}. Given that both Mg^{2+} and Ni^{2+} are divalent and Mg–O and Ni–O bonds also have similar lengths of about 2.1 Å, we suggest that the different nature of Mg–O (more ionic) and Ni–O (more covalent) bonds may be responsible for the discrepancy, and a full understanding would merit future investigations.

Conclusions

To fast predict the NMR chemical shift of paramagnetic battery materials within DFT accuracy, we presented a machine learning (ML) model, named NN-NMR model that is based on local structure descriptors and a Neural Network (NN). For validation, the NN-NMR model predicted the ^{23}Na shift of P2-type $Na_{2/3}(Mg_{1/3}Mn_{2/3})O_2$ with high accuracy compared to the DFT values. The NN-NMR model enables us to calculate the chemical shifts of a supercell model with 88 atoms within tens of milliseconds on a GPU, reducing the computational time by several orders of magnitude compared to that of the DFT method on CPUs. Also, its computational cost scales linearly with the No. of atoms, and thus the model can be readily applied to very large systems.

We further developed a novel machine learning (ML) protocol to calculate the dynamic NMR shift with DFT accuracy, which combines the machine learning potential (MLP) model and NN-NMR model for accelerating the configurational sampling and chemical shift prediction, respectively. Thanks to sufficient sampling of both configurations and chemical shifts during 200 nanoseconds (ns) MLPMD simulations, the dynamic ^{23}Na shifts of P2-$Na_{2/3}(Mg_{1/3}Mn_{2/3})O_2$ and P2-$Na_{2/3}(Ni_{1/3}Mn_{2/3})O_2$ calculated with the ML protocol have negligible statistical errors and agree with our ^{23}Na MAS NMR experimental results. Consequently, two experimental ^{23}Na shifts of P2-$Na_{2/3}(Ni_{1/3}Mn_{2/3})O_2$ were assigned to the dynamic averaged ^{23}Na NMR signal in two stacking sequences of transition metal (TM) layers, *i.e.*, space group $P6_322$ (1493 ppm) and $P6_3/mcm$ (1406 ppm), and their fractions were quantified to be 0.82 and 0.18 for the first time, respectively. Besides, comparing the diffusion channels and coefficients of Na^+ in P2-$Na_{2/3}(Mg_{1/3}Mn_{2/3})O_2$ and P2-$Na_{2/3}(Ni_{1/3}Mn_{2/3})O_2$ obtained from MLPMD simulations, we found that Mg^{2+} has a blockage effect on Na^+ diffusion while Ni^{2+} has not.

To decouple the effects between local environments and dynamic information behind dynamic NMR spectra, the ML protocol presented here can be easily extended to other fast dynamic systems, such as solutions, diamagnetic solid-state electrolytes (SSEs), *etc.*, and to other nuclei, which will stimulate future work.

Data availability

The python workflow and raw datasets for training and testing the NN-NMR model of P2-type $Na_{2/3}(Mg_{1/3}Mn_{2/3})O_2$ are available at **https://github.com/chenggroup/nmr** upon request.

Author contributions

M. L. and J. C. designed research. J. C. and Y. Y. supervised the project. M. L., J. X., F. W. and Y. H. developed and encoded the ML protocol. M. L. conducted the NMR shift calculations, DFT calculations, NMR and XRD experiments and data analysis. M. S. and X. L. assisted in materials synthesis. M. L. wrote the initial manuscript. J. C., R. F. and Y. Y. reviewed/edited the manuscript. All authors discussed the results and commented on the paper.

Conflicts of interest

There are no conflicts to declare.

Acknowledgements

This work is financially supported by the National Key Research and Development Program of China (Grant No. 2021YFB2401800), National Natural Science Foundation of China (Grant No. 21991151, 21991150, 21935009, 21761132030, 21861132015, 22021001, 92161113, and 91945301), and Xiamen Science and Technology Plan Project (No. 3502Z20203027). Dr Riqiang Fu acknowledges the support from the National High Magnetic Field Laboratory, which is supported by NSF Cooperative Agreement DMR-1644779 and the State of Florida.

References

1 A. Van der Ven, Z. Deng, S. Banerjee and S. P. Ong, *Chem. Rev.*, 2020, **120**, 6977–7019.
2 A. Grenier, P. J. Reeves, H. Liu, I. D. Seymour, K. Märker, K. M. Wiaderek, P. J. Chupas, C. P. Grey and K. W. Chapman, *J. Am. Chem. Soc.*, 2020, **142**, 7001–7011.
3 Z. Gong and Y. Yang, *J. Energy Chem.*, 2018, **27**, 1566–1583.
4 Z. Gong, W. Zhang, D. Lv, X. Hao, W. Wen, Z. Jiang and Y. Yang, *J. Electrochem.*, 2013, **19**, 512–522.
5 O. Pecher, J. Carretero-González, K. J. Griffith and C. P. Grey, *Chem. Mater.*, 2017, **29**, 213–242.
6 G. Zhong, Z. Liu, D. Wang, Q. Li, R. Fu and Y. Yang, *J. Electrochem.*, 2016, **22**, 231–243.

7 A. J. Pell, G. Pintacuda and C. P. Grey, *Prog. Nucl. Magn. Reson. Spectrosc.*, 2019, **111**, 1–271.
8 J. Kim, D. S. Middlemiss, N. A. Chernova, B. Y. X. Zhu, C. Masquelier and C. P. Grey, *J. Am. Chem. Soc.*, 2010, **132**, 16825–16840.
9 D. S. Middlemiss, A. J. Ilott, R. J. Clément, F. C. Strobridge and C. P. Grey, *Chem. Mater.*, 2013, **25**, 1723–1734.
10 R. Pigliapochi, A. J. Pell, I. D. Seymour, C. P. Grey, D. Ceresoli and M. Kaupp, *Phys. Rev. B*, 2017, **95**, 054412.
11 A. Mondal and M. Kaupp, *J. Phys. Chem. Lett.*, 2018, **9**, 1480–1484.
12 A. Mondal, M. W. Gaultois, A. J. Pell, M. Iannuzzi, C. P. Grey, J. Hutter and M. Kaupp, *J. Chem. Theory Comput.*, 2018, **14**, 377–394.
13 A. Mondal and M. Kaupp, *Solid State Nucl. Magn. Reson.*, 2019, **101**, 89–100.
14 D. L. Smiley, D. Carlier and G. R. Goward, *Solid State Nucl. Magn. Reson.*, 2019, **103**, 1–8.
15 R. J. Clément, A. J. Pell, D. S. Middlemiss, F. C. Strobridge, J. K. Miller, M. S. Whittingham, L. Emsley, C. P. Grey and G. Pintacuda, *J. Am. Chem. Soc.*, 2012, **134**, 17178–17185.
16 Y. Zhang, A. Castets, D. Carlier, M. Ménétrier and F. Boucher, *J. Phys. Chem. C*, 2012, **116**, 17393–17402.
17 G. Mali, C. Sirisopanaporn, C. Masquelier, D. Hanzel and R. Dominko, *Chem. Mater.*, 2011, **23**, 2735–2744.
18 C. Delmas, D. Carlier, G. Ceder, M. Ménétrier and C. P. Grey, *Phys. Rev. B*, 2003, **67**, 1–14.
19 A. D. Bain, *Prog. Nucl. Magn. Reson. Spectrosc.*, 2003, **43**, 63–103.
20 M. Lin, X. Liu, Y. Xiang, F. Wang, Y. Liu, R. Fu, J. Cheng and Y. Yang, *Angew. Chem., Int. Ed.*, 2021, **60**, 12547–12553.
21 C. Delmas, J.-J. Braconnier and P. Hagenmuller, *Mater. Res. Bull.*, 1982, **17**, 117–123.
22 R. J. Clément, J. Xu, D. S. Middlemiss, J. Alvarado, C. Ma, Y. S. Meng and C. P. Grey, *J. Mater. Chem. A*, 2017, **5**, 4129–4143.
23 M. Kalapsazova, S. Ivanova, R. Kukeva, S. Simova, S. Wegner, E. Zhecheva and R. Stoyanova, *Phys. Chem. Chem. Phys.*, 2017, **19**, 27065–27073.
24 X. Wu, G.-L. Xu, G. Zhong, Z. Gong, M. J. McDonald, S. Zheng, R. Fu, Z. Chen, K. Amine and Y. Yang, *ACS Appl. Mater. Interfaces*, 2016, **8**, 22227–22237.
25 G. Singh, N. Tapia-Ruiz, J. M. Lopez del Amo, U. Maitra, J. W. Somerville, A. R. Armstrong, J. Martinez de Ilarduya, T. Rojo and P. G. Bruce, *Chem. Mater.*, 2016, **28**, 5087–5094.
26 G. Singh, J. M. López del Amo, M. Galceran, S. Pérez-Villar and T. Rojo, *J. Mater. Chem. A*, 2015, **3**, 6954–6961.
27 E. Gonzalo, M. H. Han, J. M. López del Amo, B. Acebedo, M. Casas-Cabanas and T. Rojo, *J. Mater. Chem. A*, 2014, **2**, 18523–18530.
28 J. Cabana, N. A. Chernova, J. Xiao, M. Roppolo, K. A. Aldi, M. S. Whittingham and C. P. Grey, *Inorg. Chem.*, 2013, **52**, 8540–8550.
29 I. R. Mukhamedshin, H. Alloul, G. Collin and N. Blanchard, *Phys. Rev. Lett.*, 2004, **93**, 167601.
30 O. H. Han, J. K. Jung, M.-Y. Yi, J. H. Kwak and Y. J. Shin, *Solid State Commun*, 2000, **117**, 65–68.
31 J. Zhang, W. Wang, W. Wang, S. Wang and B. Li, *ACS Appl. Mater. Interfaces*, 2019, **11**, 22051–22066.
32 L. Zhang, J. Han, H. Wang, R. Car and W. E, *Phys. Rev. Lett.*, 2018, **120**, 143001.
33 Y. Zhang, H. Wang, W. Chen, J. Zeng, L. Zhang, H. Wang and W. E, *Comput. Phys. Commun.*, 2020, **253**, 107206.
34 J. Huang, L. Zhang, H. Wang, J. Zhao, J. Cheng and W. E, *J. Chem. Phys.*, 2021, **154**, 094703.
35 L. Zhang, J. Han, H. Wang, W. A. Saidi, R. Car and W. E, *Adv. Neural Inform. Process. Syst.*, 2018, **2018**, 4436–4446.
36 A. P. Bartók, R. Kondor and G. Csányi, *Phys. Rev. B*, 2013, **87**, 184115.
37 F. M. Paruzzo, A. Hofstetter, F. Musil, S. De, M. Ceriotti and L. Emsley, *Nat. Commun.*, 2018, **9**, 4501.
38 J. Vergnet, M. Saubanère, M.-L. Doublet and J.-M. Tarascon, *Joule*, 2020, **4**, 420–434.
39 M. Ben Yahia, J. Vergnet, M. Saubanère and M.-L. Doublet, *Nat. Mater.*, 2019, **18**, 496–502.
40 K. Dai, J. Wu, Z. Zhuo, Q. Li, S. Sallis, J. Mao, G. Ai, C. Sun, Z. Li, W. E. Gent, W. C. Chueh, Y. Chuang, R. Zeng, Z. Shen, F. Pan, S. Yan, L. F. J. Piper, Z. Hussain, G. Liu and W. Yang, *Joule*, 2019, **3**, 518–541.
41 U. Maitra, R. A. House, J. W. Somerville, N. Tapia-Ruiz, J. G. Lozano, N. Guerrini, R. Hao, K. Luo, L. Jin, M. A. Pérez-Osorio, F. Massel, D. M. Pickup, S. Ramos, X. Lu, D. E. McNally, A. V. Chadwick, F. Giustino, T. Schmitt, L. C. Duda, M. R. Roberts and P. G. Bruce, *Nat. Chem.*, 2018, **10**, 288–295.
42 C. Delmas, *Adv. Energy Mater.*, 2018, **8**, 1–9.
43 V. G. Malkin, M. Kaupp and M. Bühl, *Calculation of NMR and EPR Parameters*, Wiley-VCH Verlag GmbH & Co. KGaA, Weinheim, 2004.
44 G. Kresse and J. Hafner, *Phys. Rev. B*, 1993, **47**, 558–561.
45 G. Kresse and J. Furthmüller, *Phys. Rev. B*, 1996, **54**, 11169–11186.
46 P. E. Blöchl, *Phys. Rev. B*, 2000, **62**, 6158–6179.
47 R. Declerck, E. Pauwels, V. Van Speybroeck and M. Waroquier, *Phys. Rev. B*, 2006, **74**, 245103.
48 F. Han, *Problems in Solid State Physics with Solutions*, 2012, vol. 50, pp. 391–396.
49 J. P. Perdew, K. Burke and M. Ernzerhof, *Phys. Rev. Lett.*, 1996, **77**, 3865–3868.
50 J. Sun, A. Ruzsinszky and J. Perdew, *Phys. Rev. Lett.*, 2015, **115**, 036402.
51 Y. S. Meng, Y. Hinuma and G. Ceder, *J. Chem. Phys.*, 2008, **128**, 104708.
52 D. H. Lee, J. Xu and Y. S. Meng, *Phys. Chem. Chem. Phys.*, 2013, **15**, 3304.
53 K. Okhotnikov, T. Charpentier and S. Cadars, *J. Cheminform.*, 2016, **8**, 17.
54 A. P. Thompson, H. M. Aktulga, R. Berger, D. S. Bolintineanu, W. M. Brown, P. S. Crozier, P. J. in't Veld, A. Kohlmeyer, S. G. Moore, T. D. Nguyen, R. Shan, M. J. Stevens, J. Tranchida, C. Trott and S. J. Plimpton, *Comput. Phys. Commun.*, 2022, **271**, 108171.
55 J. R. Kermode, *J. Phys. Condens. Matter*, 2020, **32**, 305901.

56 M. Abadi, A. Agarwal, P. Barham, E. Brevdo, Z. Chen, C. Citro, G. S. Corrado, A. Davis, J. Dean, M. Devin, *et al.*, *TensorFlow: Large-Scale Machine Learning on Heterogeneous Systems*, 2015, **https://www.tensorflow.org/**.
57 F. Chollet, *Keras*, 2015, **https://keras.io**.
58 L. Kahle, A. Musaelian, N. Marzari and B. Kozinsky, *Phys. Rev. Mater.*, 2019, **3**, 055404.
59 C. Bonhomme, C. Gervais, F. Babonneau, C. Coelho, F. Pourpoint, T. Azaïs, S. E. Ashbrook, J. M. Griffin, J. R. Yates, F. Mauri and C. J. Pickard, *Chem. Rev.*, 2012, **112**, 5733–5779.
60 W. Zuo, J. Qiu, C. Hong, X. Liu, J. Li, G. F. Ortiz, Q. Li, S. Zheng, G. R. Zheng and Y. Yang, *ACS Appl. Energy Mater.*, 2019, **2**, 4914–4924.
61 Z. Lu and J. R. Dahn, *J. Electrochem. Soc.*, 2001, **148**, A1225.
62 J. Cabana, N. A. Chernova, J. Xiao, M. Roppolo, K. A. Aldi, M. S. Whittingham and C. P. Grey, *Inorg. Chem.*, 2013, **52**, 8540–8550.
63 N. Tapia-Ruiz, W. M. Dose, N. Sharma, H. Chen, J. Heath, J. W. Somerville, U. Maitra, M. S. Islam and P. G. Bruce, *Energy Environ. Sci.*, 2018, **11**, 1470–1479.
64 X. He, Y. Zhu, A. Epstein and Y. Mo, *npj Comput. Mater.*, 2018, **4**, 18.